(Received 25 September 2024, Accepted 13 November 2024, Scheduled 21 November 2024)

# Analysis of Eddy Current Losses and Stresses in High-Speed Permanent Magnet Synchronous Motors with Frameless Torque

Xiping Liu, Haiao Sun*, Zhangqi Liu, and Canwei Zhang

*School of Electricity and Automation, Jiangxi University of Science and Technology, Ganzhou 341000, Jiangxi, China*

**ABSTRACT:** In this paper, a high-speed frameless torque permanent magnet synchronous motor is designed to determine the optimal structure of the rotor by comparing the air gap magnetism, cogging torque, and output torque of the motor through finite element analysis. The effects of different material rotor sheaths on eddy current loss are compared and analyzed, and the copper shield is used to optimize the rotor eddy current loss of the high-speed frameless torque motor. Through the analytical method, based on the theory of thick-walled cylinder, the stress calculation is carried out on the multilayer rotor structure of the high-speed permanent magnet synchronous motor with copper shielding layer, and a comparative analysis is carried out with the simulation results to verify the validity of the analytical calculations and the reasonableness of the optimization of the rotor eddy current loss.

## 1. INTRODUCTION

Compared with traditional permanent magnet motors, frameless torque motors are characterized by a simple and compact structure.d Refs. [1, 2] optimize the electromagnetic characteristics of frameless torque motors by analytical method and experiments, and deeply analyze that frameless torque motors are widely used in the field of robot joint motors by virtue of higher power density and lower torque density. Ref. [3] analyzes the characteristics of frameless torque motors during high-speed operation, which are able to provide high power output in a more lightweight and low-inertia manner than ordinary high-speed permanent magnet synchronous motors. Refs. [4, 5] analyze the operating characteristics of conventional permanent magnet motors and high-speed permanent magnet synchronous motors, and obtains that high-speed permanent magnet synchronous motors have been widely used and researched because of their high power density, small size, high operating efficiency, and high reliability. The eddy current losses and rotor stresses generated by permanent magnet synchronous motors during high-speed operation have always been the focus and difficulty in the study of high-speed permanent magnet motors.

Scholars have carried out many studies on the loss analysis and rotor stress of high-speed permanent magnet motors. Ref. [6] comparatively analyzes the electromagnetic characteristics of high-speed motors with rare earth permanent magnets and ferrite permanent magnets. Refs. [7, 8] analyze the effect of different pole-slot fits on the electromagnetic characteristics of high-speed motors. Ref. [9] analyzes the effect of different overfilling methods of the rotor on the rotor stress of high speed motors by finite element method. Ref. [10] studies and analyzes the rotor strength and sheath design of high-speed permanent magnet synchronous motor by establishing a two-dimensional analytical model for analytical calculation. Ref. [11] uses analytical method and finite element method to study the rotor stress distribution law of sheath axial segmented structure and the influence law of the number of sheath segments on the rotor strength. Refs. [12, 13] deduce the analytical calculation formulas for the strain field, displacement field, and stress field of the rotor of a high-speed permanent magnet motor, verify the correctness of the analytical calculations by using the finite element method, and analyze the influencing factors of the rotor strength. Ref. [14] studies the distribution characteristics and changing law of three-dimensional electromagnetic field and eddy current loss of low temperature high-speed permanent magnet motor. Ref. [15] based on the proposed field-circuit coupling method obtains the high-speed motor rotor loss characteristics and proposes an electromagnetic-thermal iterative calculation method to analyze the temperature distribution. Refs. [16–18] propose an analytical model of the rotor eddy current loss of a high-speed permanent magnet synchronous motor and compare the analytical results, finite element results, and experimental results to prove the correctness of the proposed analytical model. Ref. [19] investigates the effectiveness of increasing the resistivity of permanent magnets in reducing the rotor eddy current loss of high-speed permanent magnet motors. Ref. [20] investigates the effect of different driving modes on the losses of high-speed permanent magnet synchronous motors.

From the above research status, many scholars have studied high-speed permanent magnet synchronous motors from electromagnetic characteristics, loss analysis, or rotor strength of a certain discipline, which is lack of comprehensive. In this paper, we will analyze the high-speed permanent magnet synchronous motor from the electromagnetic characteristics, eddy current loss and stress analysis, multidisciplinary and multi-angle comprehensive research. In this paper, the optimal structure of the rotor of a high-speed frameless torque permanent

* Corresponding author: Haiao Sun (2217527052@qq.com).

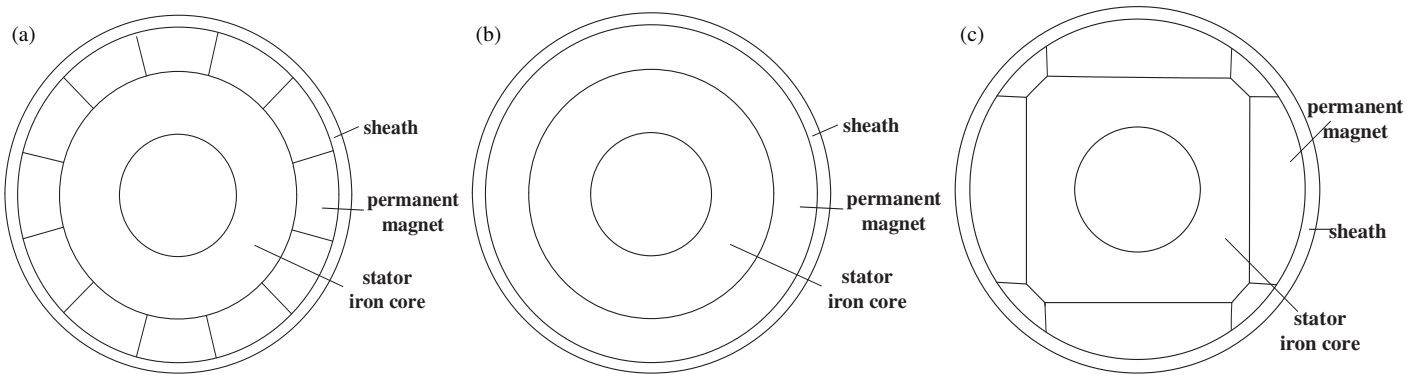


**FIGURE 1**. Shape of rotor permanent magnets for common high-speed motors, (a) segmented-typ, (b) ring-type, (c) bread-type.

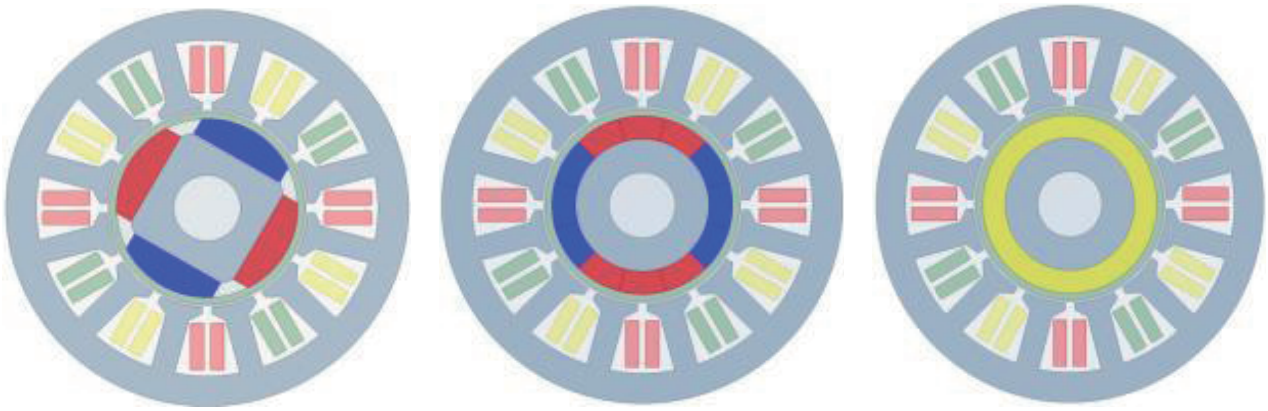

**FIGURE 2**. Simulation model of motor with different rotor structures.

magnet synchronous motor is determined by comparing the air gap magnetic density, cogging torque, and output torque of the motor through finite element analysis. The effects of carbon fiber sheath and alloy sheath on eddy current loss are compared and analyzed, and the suppression effect of copper shielding layer on eddy current loss of high-speed frameless torque motor rotor is studied and analyzed. Based on the theory of thick-walled cylinder, the stress analysis calculation is carried out on the high-speed permanent magnet synchronous motor with multi-layer rotor structure of sheath, copper shielding layer, and permanent magnet, and the simulation results are compared and analyzed with the simulation results of stress analysis of workbench, which verifies the validity of the stress analysis calculation and the reasonableness of the optimization of eddy-current loss of the rotor with copper shielding layer.

## 2. ROTOR STRUCTURE DESIGN

Rotor design is the key technology of high-speed permanent magnet synchronous motor, and NdFeB and SmCo are commonly used permanent magnet materials for high-speed motors. Permanent magnet has strong compression resistance but weak tensile resistance, and the motor will generate a lot of centrifugal force when running at high speed, so it needs a jacket to protect the permanent magnet. High-speed permanent magnet motors have fewer poles, usually 1 pair of poles and 2 pairs of poles. 1 pair of poles of the stator winding end of the motor is longer, and the stator yoke and teeth are wider, resulting in greater copper consumption of the motor, so in this paper, we will use the 2 pairs of poles rotor structure. High-speed motors mostly use a surface-mounted structure, and there are mainly bread-type, segmented-type, and ring-type rotor permanent magnet shapes, as shown in Fig. 1. In this paper, we will take a frameless torque permanent magnet synchronous motor with rated power of 5 KW and maximum speed of 20000 r/min as the research object, and the specific motor parameters are shown in Fig. 1.

The basic stator and rotor dimensions are determined, and the amount of permanent magnets is controlled to be the same. The simulation models of motors with different rotor structures are constructed as shown in Fig. 2. The constructed simulation model is subjected to Maxwell finite element simulation under rated operating conditions, and the no-load air gap magnetization is obtained as shown in Fig. 3. The Fourier decomposition of the no-load air gap magnetization waveforms of the three different rotor structures is carried out, and the various harmonic components are obtained as shown in Fig. 4. As known from Fig. 3 and Fig. 4, the air-gap magnet density waveform of the toroidal permanent magnet structure has the least harmonics and the best sinusoidality.

Figure 5 shows the simulation results of the cogging torque of the motor model with different rotor structures, and it can

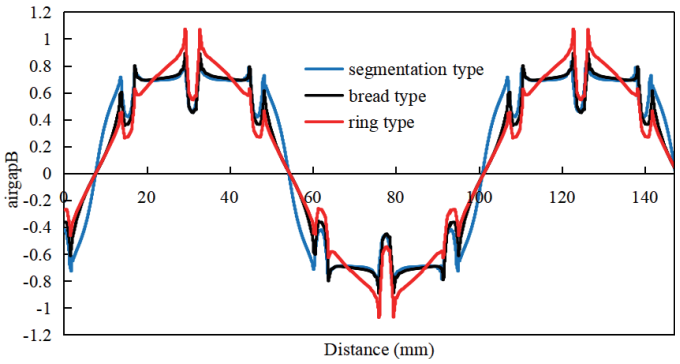


**FIGURE 3**. Comparison of unloaded air gap magnetic density waveforms.

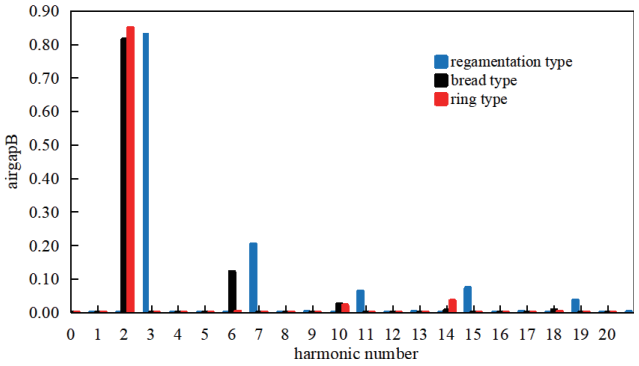


**FIGURE 4**. Comparison of the various harmonics of the unloaded air-gap magnetic density waveforms.

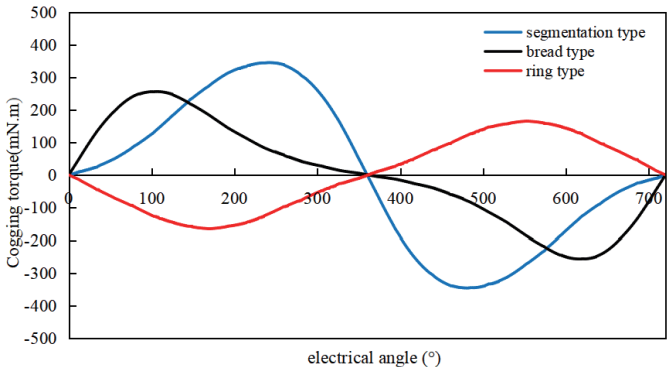


**FIGURE 5**. Comparison of gearing torque.

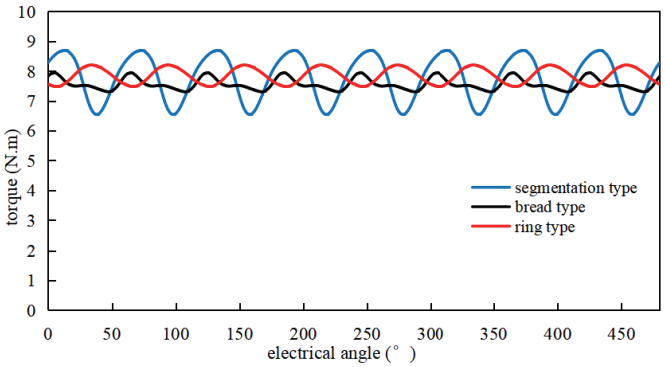


**FIGURE 6**. Comparison of output torque.

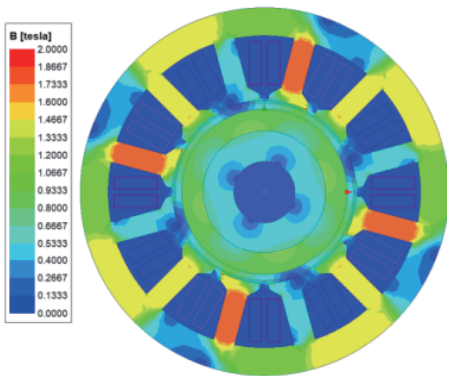


**FIGURE 7**. Flux density distribution of the motor.

**TABLE 1**. Motor parameters.

| Motor parameters | parameter value |
|---|---|
| Outer diameter of stator (mm) | 120 |
| Inner diameter of stator (mm) | 60 |
| Length of air gap (mm) | 1 |
| Sheath thickness (mm) | 5 |
| Permanent magnet thickness (mm) | 7 |
| Pole/Slot | 4/12 |
| Rated power (KW) | 5 |
| Rated speed (r/min) | 17000 |
| Core length (mm) | 80 |

be seen from the figure that the lowest cogging torque is 165.65 mN·m for the toroidal permanent magnetstructure.

Figure 6 shows the comparison of the output torque waveforms of three different rotor structures with load, and the specific data of the average output torque and torque pulsation of the bread-type, segmented-type, and ring-type permanent magnet structures are shown in Table 2, which is obtained from Table 1, the output torque of the ring permanent magnet is larger at 7.84 N·m, and that of the bread-type and ring-type permanent magnets is smaller, and the difference is not large at 8.48% and 9.18%.

In this section, three high-speed permanent magnet synchronous motor models with different rotor structures are constructed, and the simulation results of air-gap magnetic density, cogging torque, and output torque electromagnetic characteristics of the motor are compared by Maxwell finite element analysis to determine that the permanent magnet rotor structure of ring-type is the optimal structure for the high-speed frameless torque permanent magnet synchronous motor rotor. Fig. 7 shows the flux density distribution of the motor, and the flux densities of the tooth part and yoke part are 1.7 T and 1.5 T, respectively, which are not saturated and satisfy the basic operation requirements.

**TABLE 2**. Average output torque and torque pulsation.

| permanent magnet structure | bread type | segmented type | ring type |
|---|---|---|---|
| average output torque (mN·m) | 7.56 | 7.77 | 7.84 |
| torque pulsation | 8.48% | 27.67% | 9.18% |

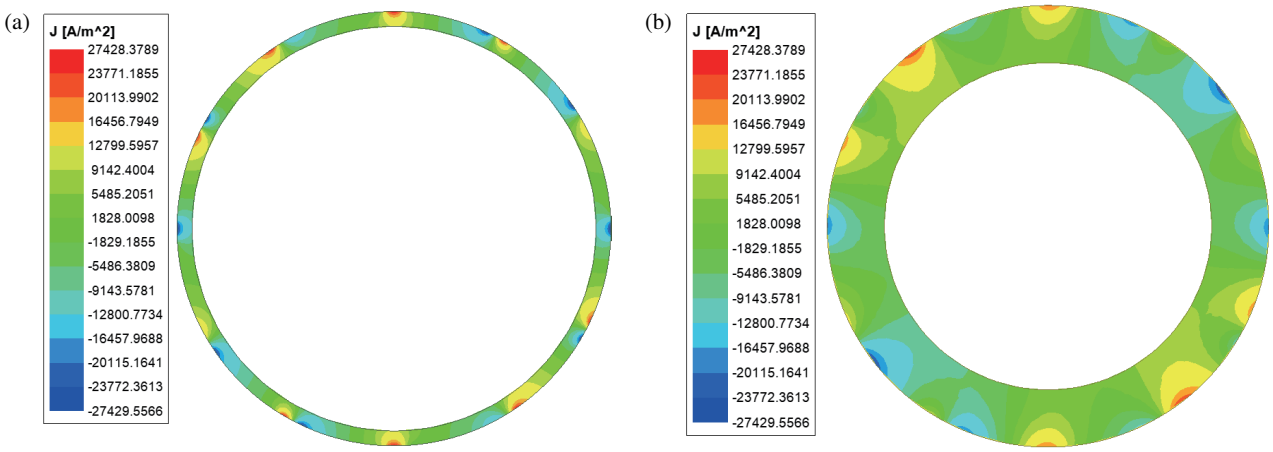


**FIGURE 8**. Carbon fiber sheathed rotor eddy current density distribution. (a) Carbon fiber sheath eddy current density distribution. (b) Permanent magnet eddy current density distribution.

## 3. EDDY CURRENT LOSS ANALYSIS

Changes in the magnetic kinetic potential due to the cogging effect of the stator slot openings in a permanent magnet synchronous motor, the non-sinusoidal distribution of the winding magnetic potential, and the space and time harmonics in the winding currents produce eddy-current losses in the rotor, which are concentrated on the surface of the magnetic poles. The eddy current loss will produce a larger eddy current density on the surface of the magnetic poles, generating higher temperatures, which may lead to local demagnetization of the permanent magnets in severe cases. In common medium and low-speed permanent magnet synchronous motors, the eddy current loss of the rotor is often negligible, but in high-speed permanent magnet synchronous motors, due to the high frequency and significant skin effect, the eddy current loss of the motor is more obvious. Therefore, the optimization study of eddy current loss in high-speed permanent magnet motors is of great significance to the development of motor design.

High-speed permanent magnet synchronous motor commonly used sheath for carbon fiber and alloy, because the conductivities of the two materials differ greatly, so the impact on the rotor eddy current loss is not the same. In this section, we mainly study the effect of different material sheaths on the rotor eddy current loss and then optimize the design of rotor loss by adding copper shielding layer between the sheath and the permanent magnet.

The eddy current loss of the sheath and permanent magnet is calculated as shown in the following equation:

$$P = i^2 r = (JS)^2 \rho \frac{l}{S} = \rho l \iint J^2 ds \tag{1}$$

where $\rho$ is the resistivity of the permanent magnet and the sheath material, $\Omega \cdot$ m; $J$ is the induced current density in the material, A/m$^2$; $S$ is the end surface area of the material, m$^2$; $l$ is the axial length of the material, $m$.

Finite element loss simulation analysis was performed for the two sheath materials identified above for the ring-type permanent magnet rotor structure, carbon fiber sheath, and alloy material sheath, and the eddy current densities of the permanent magnet and the sheath for the two sheath materials are shown in Figs. 8 and 9.

As can be seen from the above figure, the eddy current density in the carbon fiber sheath is similar to the eddy current loss density in its permanent magnet, which is $2.74 \times 10^4$ A/m$^2$. The eddy current density in the alloy sheath is $5.55 \times 10^5$ A/m$^2$, and the eddy current density of its permanent magnet is $2.26 \times 10^4$ A/m$^2$. As can be seen in Eq. (1), the rotor eddy current loss is directly proportional to the square of the eddy current density, and therefore the eddy current loss of the alloy sheath is much greater than that of carbon fiber sheath. Since the conductivity of alloy $6.1 \times 10^5$ S/m is much larger than that of carbon fiber $3.0 \times 10^4$ S/m, to a certain extent, the larger the conductivity of the sheath is, the stronger the eddy current effect is in the sheath, the larger the eddy current loss is, and the stronger the inhibition of eddy current loss is in the permanent magnet, which effectively prevents the permanent magnet from excessive eddy current loss and high local temperature leading to demagnetization.

Based on the effect of the sheath conductivity on the eddy current loss of the permanent magnet, a copper shielding layer with a conductivity of $5.8 \times 10^7$ S/m can be further added between the sheath and permanent magnet to reduce the eddy cur-

**TABLE 3**. Comparison of eddy current losses.

| Materials | carbon fiber | alloys | with copper shielding |
|---|---|---|---|
| Maximum value of J in the sheath ($A/m^{2)}$ | $2.74 \times 10^4$ | $5.55 \times 10^5$ | $1.99 \times 10^7$ |
| Maximum value of J in the PM ($A/m^{2)}$ | $2.74 \times 10^4$ | $2.26 \times 10^4$ | $1.91 \times 10^4$ |
| Sheath Eddy Current Loss (w) | 6.97 | 14.18 | 37.40 |
| Permanent Magnet Eddy Current Losses (w) | 8.27 | 5.34 | 1.91 |

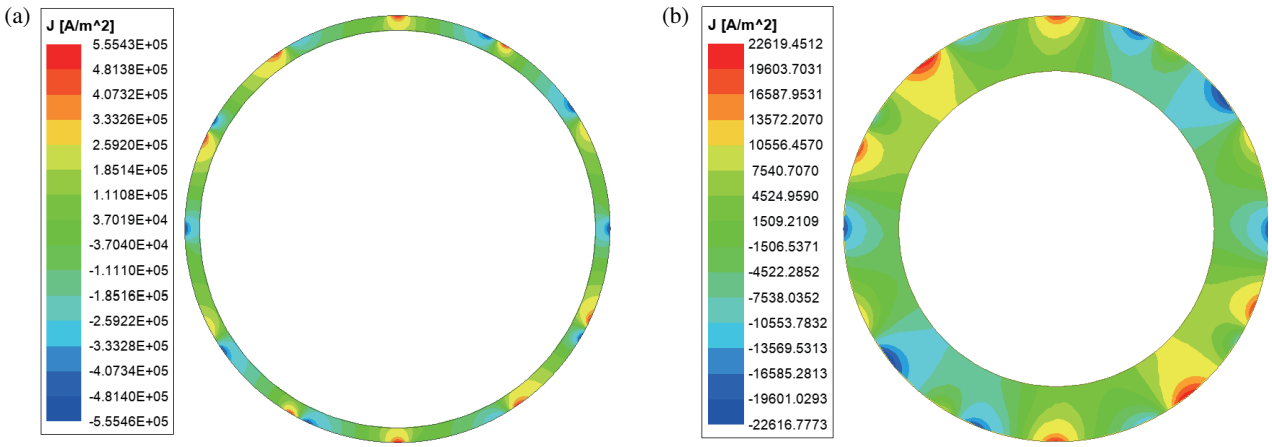


**FIGURE 9**. Distribution of eddy current density of alloy material sheathed rotor. (a) Eddy current density distribution of alloy materials. (b) Permanent magnet eddy current density distribution.

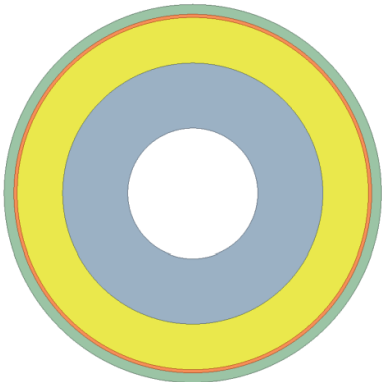

**FIGURE 10**. Rotor structure with copper shielding.

rent loss in the permanent magnet. The rotor model with copper shielding layer is shown in Fig. 10, and the eddy current density finite element simulation results are shown in Fig. 11.

As can be seen from the above figure, due to the addition of a larger conductivity copper shielding layer between the permanent magnet and alloy sheath, the eddy current density of $1.99\times10^7$ A/m$^2$ in the copper shielding layer is generated much larger than that in the alloy sheath, which suppresses the eddy current effect in the permanent magnet and greatly reduces the eddy current density of $1.91 \times 10^4$ A/m$^2$ in the permanent magnet. The eddy current loss of the sheathed rotor of different materials can be derived from Eq. (1) as shown in Table 3, from which it can be seen that the structure of the sheathed rotor with copper shielding layer can effectively suppress the eddy current loss.

In this section, the effect of material conductivity on the eddy current density in the sheath and permanent magnet is analyzed by comparing the rotor eddy current losses in the carbon fiber sheath and the alloy material sheath. By adding a copper shielding layer between the permanent magnet and alloy sheath, the eddy current effect in the permanent magnet is further weakened; the eddy current loss in the permanent magnet is reduced; and the permanent magnet eddy localized temperature is prevented from being too high leading to demagnetization, which affects the normal work operation of the motor. However, it can be seen from the above figure that the use of higher conductivity sheaths and shields may result in higher eddy current losses, higher temperature rise, and larger deformation during high-speed operation. And the addition of the copper shielding layer causes a large change in the rotor structure, so it is necessary to accurately calibrate the stress distribution of the rotor during high-speed operation.

## 4. MULTILAYER ROTOR STRUCTURE STRESS ANALYSIS

### 4.1. Analytical Calculation of Rotor Stress

The main purpose of rotor stress analysis is to verify whether a rotor structure is able to withstand the permitted stresses to ensure the safety of the motor in high-speed operation. Since it is extremely difficult to measure the strain and stress of the

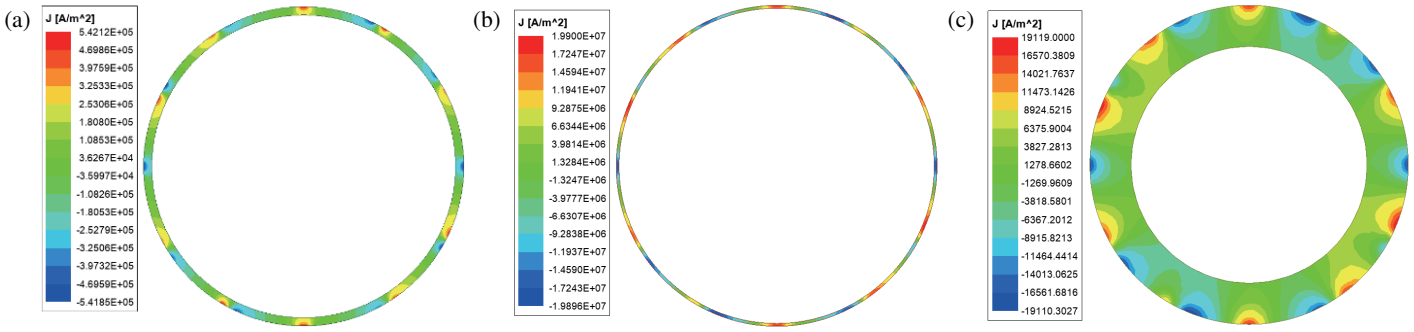


**FIGURE 11**. Eddy current density distribution of rotor with copper shielding layer. (a) Distribution of eddy current losses in alloy sheaths. (b) Distribution of eddy current losses in the copper shielding layer. (c) Permanent magnet eddy current loss distribution.

rotor when the motor is running at high speed, the analytical method is used to analyze the rotor strength of high-speed permanent magnet synchronous motor. In the above, due to the optimization of eddy current loss, a copper shielding layer is added between the permanent magnet and the sheath, forming a multi-layer rotor structure with mutual interference fit of rotor shaft — permanent magnet — copper shielding layer — sheath, which makes the stresses on the rotor change considerably compared with the traditional high-speed permanent magnet synchronous motor. Based on the theoretical model of thick-walled cylinder, this paper will derive the analytical formula of the stress on the multilayer rotor structure of the high-speed motor and analyze the analytical value in comparison with the stress result of the workbench simulation, so as to verify the safety of the motor in the high-speed operation at the maximum speed. The two-dimensional model of the multilayer rotor structure of the high-speed permanent magnet synchronous motor is shown in Fig. 12.

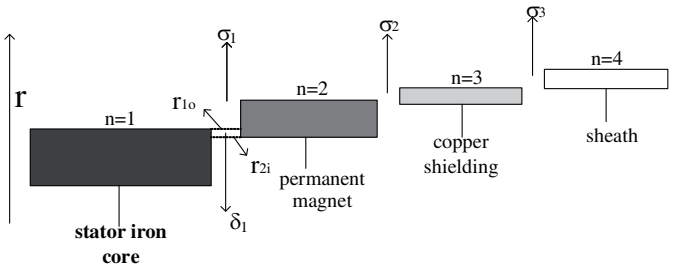


**FIGURE 12**. 2D model of multilayer rotor structure.

Let the rotor of a high-speed motor consist of an $n$-layer structure, with $n$ gradually increasing from inside to outside, and the $n$-layer structure has a total of $n-1$ contact surfaces with an interference fit between them. $r_{no}$ is the outer diameter of the $n$th layer structure, and $r_{ni}$ is the inner diameter of the $n$th layer structure. The amount of interference fits between the $n$th and $n+1$st layers is $\delta_n$, and the compressive stress between the $n$th and $n+1$st layers is $\sigma_n$

$$u_{no} - u_{n+1i} = \delta_n \tag{2}$$

$u_{no}$ is the displacement of the outer diameter of the $n$th layer of the structure, and $u_{n+1i}$ is the displacement of the inner diameter of the $n+1$st layer of the structure.

Hooke's law considering the change in temperature rise at high speed operation of the motor is:

$$\begin{cases} \varepsilon_{rn} = \dfrac{\sigma_{rn}}{E_{rn}} - \dfrac{\mu_{\theta rn}\sigma_{\theta n}}{E_{\theta n}} + \beta_{rn}\Delta T \\ \varepsilon_{rn} = \dfrac{\sigma_{\theta n}}{E_{\theta n}} - \dfrac{\mu_{r\theta n}\sigma_{\theta n}}{E_{rn}} + \beta_{\theta n}\Delta T \end{cases} \tag{3}$$

$\varepsilon_{rn}$ and $\varepsilon_{\theta n}$ are radial and tangential strains; $\sigma_{rn}$ and $\sigma_{\theta n}$ are radial and tangential stresses; $E_{rn}$ and $E_{\theta n}$ are radial and tangential moduli of elasticity; $\mu_{r\theta n}$ and $\mu_{\theta rn}$ are radial and tangential Poisson's ratios; $\beta_{rn}$ and $\beta_{\theta n}$ are coefficients of thermal expansion in the radial and tangential directions; $\Delta T$ is the temperature rise of the rotor; and $n$ is the rotor structural sequence number.

From the thick-walled cylinder theory, the geometric equation for strain-displacement is:

$$\begin{cases} \varepsilon_{rn} = \dfrac{du_n}{dr} \\ \varepsilon_{\theta n} = \dfrac{u_n}{r} \end{cases} \tag{4}$$

$u_n$ and $r$ are the $n$-story structural displacement and radius position, respectively.

According to the theory of elastic mechanics, the equilibrium differential equations for each layer of the rotor structure are as follows:

$$\frac{d\sigma_{rn}}{d_r} + \frac{\sigma_{rn} - \sigma_{\theta n}}{r} + \rho_n \omega^2 r = 0 \tag{5}$$

$\rho_n$ is the density of the nth rotor structure, and $\omega$ is the rotational angular velocity.

The stress differential equation is obtained by associating Eqs. (3)–(5):

$$\begin{cases} \sigma_{rn} = \dfrac{E_{rn}}{1-\mu_{\theta rn}\mu_{r\theta n}}\Big(\dfrac{du_n}{dr}+ \\ \qquad \mu_{\theta rn}\dfrac{u_n}{r} - \beta_{rn}T - \mu_{\theta rn}\beta_{\theta n}T\Big) \\ \sigma_{rn} = \dfrac{E_{\theta n}}{1-\mu_{r\theta n}\mu_{\theta rn}}\Big(\dfrac{u_n}{r}+ \\ \qquad \mu_{r\theta n}\dfrac{du_n}{dr} - \beta_{\theta n}T - \mu_{r\theta n}\beta_{rn}T\Big) \end{cases} \tag{6}$$

Associate Eqs. (5), (6):

$$\begin{aligned} & E_{rn}r^2\frac{d^2_{u_n}}{dr^2} + E_{rn}r\frac{du_n}{dr} - E_{rn}r\frac{du_n}{dr} - E_{\theta n}u_n \\ =& (E_{rn} - E_{\theta n}\mu_{r\theta n})\beta_{rn}Tr + (E_{rn} - E_{\theta n}) \\ & E_{\theta n}\times Tr + E_{rn}r^2(\beta_{rn} + \beta_{\theta n}\mu_{\theta rn})\frac{d\Delta T}{dr} \\ & - \rho_n\omega^2 r^3(1-\mu_{\theta rn}\mu_{r\theta n}) \end{aligned} \tag{7}$$

Solving the differential Eq. (5) yields an expression for the $n$th layer structural displacement $u_n(r)$:

$$\begin{aligned} u_n(r) =& A_n r^k + B_n r^{-k} \\ & + \frac{\rho n\omega^2(1-\mu_{\theta rn}\mu_{r\theta n})r^3}{E_{rn}(k^2-9)} \\ & + \frac{(\beta_{rn}\mu_{r\theta n} + \beta_{\theta n}k^2 - \beta_{\theta n}\mu_{\theta rn} - \beta_{rn})C_{1n}}{2k} \\ & + \frac{(\beta_{\theta n}\mu_{\theta rn} + \beta_{rn})C_{2n}}{2k} \end{aligned} \tag{8}$$

where *An* and *Bn* are the coefficients to be determined.

$$\begin{aligned} k &= \sqrt{\frac{E_\theta}{E_r}} \\ C_{1n} &= \Big(\int_{R_{ni}}^{r} Tr^k dr\Big)r^{-k} - \Big(\int_{R_{ni}}^{r} Tr^{-k}dr\Big)r^k) \\ C_{2n} &= \Big(\int_{R_{ni}}^{r} r^{-k-1}\Big(\frac{d\Delta T}{dr}\Big)dr\Big)r^k \\ & \quad - \Big(\int_{R_{ni}}^{r} r^{k+1}\Big(\frac{d\Delta T}{dr}\Big)dr\Big)r^{-k} \end{aligned} \tag{9}$$

Substituting Eq. (8) into Eq. (6) yields the following expressions for the radial and tangential stresses in the $n$th layer of the structure:

$$\begin{cases} \sigma_{rn} = \dfrac{E_{rn}}{1-\mu_{\theta rn}\mu_{r\theta n}}\{A_n(k+\mu_{\theta rn})r^{k-1} \\ + B_n(\mu_{\theta rn}-k)r^{-k-1} + \dfrac{C_{3n}(\beta_{\theta n}\mu_{\theta rn}+\beta_{rn})}{2k} \\ + \dfrac{C_{4n}\left[(\beta_{rn}\mu_{r\theta n}+\beta_{rn})k^2 - \beta_{\theta n}\mu_{\theta rn} - \beta_{rn}\right]}{2k} \\ + \dfrac{\rho_n\omega^2(1-\mu_{\theta rn}\mu_{r\theta n})(3+\mu_{\theta rn})r^2}{E_{rn}(k^2-9)} \\ - (\beta_{rn}+\beta_{\theta n}\mu_{\theta rn})\Delta T\} \\ \sigma_{\theta n} = \dfrac{E_{\theta n}}{1-\mu_{\theta rn}\mu_{r\theta n}}\{A_n(1+k\mu_{r\theta n})r^{k-1} \\ + B_n(1-k\mu_{r\theta n})r^{-k-1} + \dfrac{C_{5n}(\beta_{\theta n}\mu_{\theta rn}+\beta_{rn})}{2k} \\ + \dfrac{C_{6n}\left[(\beta_{rn}\mu_{r\theta n}+\beta_{\theta n})k^2 - \beta_{\theta n}\mu_{\theta rn} - \beta_{rn}\right]}{2k} \\ + \dfrac{\rho_n\omega^2(1-\mu_{\theta rn}\mu_{r\theta n})(3\mu_{r\theta n}+1)r^2}{E_{rn}(k^2-9)} \\ - (\beta_{\theta n}+\beta_{rn}\mu_{r\theta n})\Delta T\} \end{cases} \tag{10}$$

$$\begin{aligned} C_{3n} &= (k+\mu_{\theta rn})r^{k-1}\left(\int_{R_{ni}}^{r} r^{-k+1}\left(\frac{d\Delta T}{dr}\right)dr\right) \\ &\quad +(k-\mu_{\theta rn})r^{-k-1}\left(\int_{R_{ni}}^{r} r^{k+1}\left(\frac{d\Delta T}{dr}\right)dr\right) \\ C_{4n} &= (\mu_{\theta rn}-k)r^{-k-1}\left(\int_{R_{ni}}^{r}\Delta T r^k dr\right) \\ &\quad -(k+\mu_{\theta rn})r^{k-1}\left(\int_{R_{ni}}^{r}\Delta T r^{-k}dr\right) \\ C_{5n} &= (1+k\mu_{r\theta n})r^{k-1}\left(\int_{R_{ni}}^{r} r^{-k+1}\left(\frac{d\Delta T}{dr}\right)dr\right) \\ &\quad +(k\mu_{r\theta n}-1)r^{-k-1}\left(\int_{R_{ni}}^{r} r^{k+1}\left(\frac{d\Delta T}{dr}\right)dr\right) \\ C_{6n} &= (1-k\mu_{r\theta n})r^{-k-1}\left(\int_{R_{ni}}^{r}\Delta T r^k dr\right) \\ &\quad -(k\mu_{\theta rn}+1)r^{k-1}\left(\int_{R_{ni}}^{r}\Delta T r^{-k}dr\right) \end{aligned}$$

The equivalent stress $\sigma$ in the $n$th layer can be expressed by the radial and tangential stresses in the following equation:

$$\sigma = \sqrt{\frac{1}{2}[(\sigma_{rn}-\sigma_{\theta n})^2 + \sigma_{rn}^2 + \sigma_{\theta n}^2]} \tag{11}$$

In order to obtain the pending coefficients $An$ and $Bn$ in the above equation, it is necessary to determine the boundary conditions for the rotor stresses. From the mechanical analysis, it can be seen that the radial force on the outer surface of the $n-1$st layer structure has the same value and magnitude as the radial force on the inner surface of the $n$th layer structure. The outer surface of the outermost sheath is not in contact with any structure, so the radial stress that it is subjected to is 0. The boundary condition for the rotor stress is:

$$\begin{cases} \sigma(r)|_{(r=r_{1o})} = \sigma(r)|_{(r=r_{2i})} = -P_1 \\ \sigma(r)|_{(r=r_{2o})} = \sigma(r)|_{(r=r_{3i})} = -P_2 \\ \cdots \\ \sigma(r)|_{(r=r_{n-1o})} = \sigma(r)|_{(r=r_{ni})} = -P_{n-1} \\ \sigma(r)|_{(r=r_{no})} = 0 \end{cases} \tag{12}$$

Considering the rotational and temperature conditions, the working static pressure between the permanent magnet and the sheath is:

$$P_n = \frac{\delta_n}{r_{ni}[\frac{1}{E_{rn}}(\frac{r_{no}^2+r_{ni}^2}{r_{no}^2-r_{ni}^2}-\mu_n)+\frac{1}{E_{rn+1}}(\frac{r_{n+1o}^2+r_{n+1i}^2}{r_{n+1o}^2-r_{n+1i}^2}-\mu_n)]} \tag{13}$$

Based on the above boundary conditions, the coefficients to be determined, $An$ and $Bn$, can be obtained. Substituting the coefficients to be determined, $An$ and $Bn$, into Eqs. (8) and (10), the radial displacements, radial stresses, tangential stresses, and equivalent stresses of the structure at each layer can be obtained.

### 4.2. Finite Element Analysis of Rotor Stress

In order to verify the validity and accuracy of the above analytical calculations, a three-dimensional model of a high-speed permanent magnet synchronous frameless torque motor is constructed as shown in Fig. 13. The finite element method of workbench software is applied to study the strength of the rotor and compared and analyzed with the results of the analytical calculation. The main parameters of the rotor are shown in Table 4.

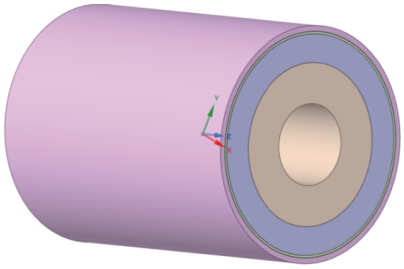

**FIGURE 13**. 3D model of high-speed motor rotor.

In order to ensure the reliability of the motor when it is running at high speed under actual working conditions, the rotational speed needs to retain a margin of 20% of the maximum

**TABLE 4**. Rotor material coefficients.

| material factor | permanent magnet | copper shield | alloy sheath |
|---|---|---|---|
| $\rho$ (kg·m$^{-3}$) | 7400 | 8942 | 8190 |
| $E_{\theta n}$ ($10^{10}$ pa) | 16 | 12.6 | 20.5 |
| $E_{rn}$ ($10^{10}$ pa) | 16 | 12.6 | 20.5 |
| $\mu_{r\theta n}$ | 0.24 | 0.345 | 0.28 |
| $\mu_{\theta rn}$ | 0.24 | 0.345 | 0.28 |
| $\beta_{rn}$ (K$^{-1}$) | $8\times10^{-6}$ | $1.67\times10^{-5}$ | $1.3\times10^{-5}$ |
| $\beta_{\theta n}$ (K$^{-1}$) | $8\times10^{-6}$ | $1.67\times10^{-5}$ | $1.3\times10^{-5}$ |

speed when the finite element simulation analysis is carried out, and this paper takes the permanent magnet synchronous motor with a maximum speed of 20000 r/min as the research target, so the speed of the stress finite element simulation should be set to 24000 r/min. The strain and high temperature generated when the rotor rotates at high speed can reduce the amount of interference between the various structures. Therefore, how to determine the amount of interference is one of the key problems to be solved in the design of high-speed permanent magnet rotor. The stress limit value that the rotor can withstand is usually determined based on the yield strength of the rotor material and the safety factor, and then determines the rotor structure interference. Add stress constraints for the rotor sheath and permanent magnet while solving for the appropriate constraints for each rotor structure thickness and overload:

$$\begin{cases} \sigma_\theta(r=r_{ni}) \le \sigma_{ni\,\max} \\ \sigma_r(r=r_{no}) \ge \sigma_{no\,\min} \end{cases} \tag{14}$$

where $\sigma_{ni\,\max}$ is the maximum tangential stress on the inner surface of the $n$th layer structure and $\sigma_{\text{nomax}}$ the minimum radial substress on the outer surface of the $n$th layer structure.

The copper shield and sheath are located between the permanent magnets and motor stator, and since the effective air gap of the motor is an important guarantee of the electromagnetic performance of the motor, the designed sheath thickness has a certain range. The sheath thickness is too small to achieve the effect of protecting the permanent magnets and too large to reduce the rated output performance of the motor, so it is necessary to determine a reasonable range of the sheath thickness at the beginning of the design and to determine the range of the amount of interference through the analytical calculations in the previous section. When designing the thickness of the sheath, it is necessary to retain a certain margin at the beginning of the design, taking into account that the motor may be overloaded, i.e., the motor speed exceeds the rated speed. The selected jacket and permanent magnet constraints are less than 75% of the tensile strength of the permanent magnet and jacket, that is, the permanent magnet, jacket, and copper shield can withstand the maximum tensile strength in accordance with the design of less than 56.25 MPa, 743.16 MPa, and 102.38 MPa, through the formula and constraints to obtain the thickness of the jacket which should be between 1.5 and 3 mm. The thickness of copper shielding should be between 0.48 and 0.80 mm, and the interference should be between 0.08 mm and 0.14 mm.

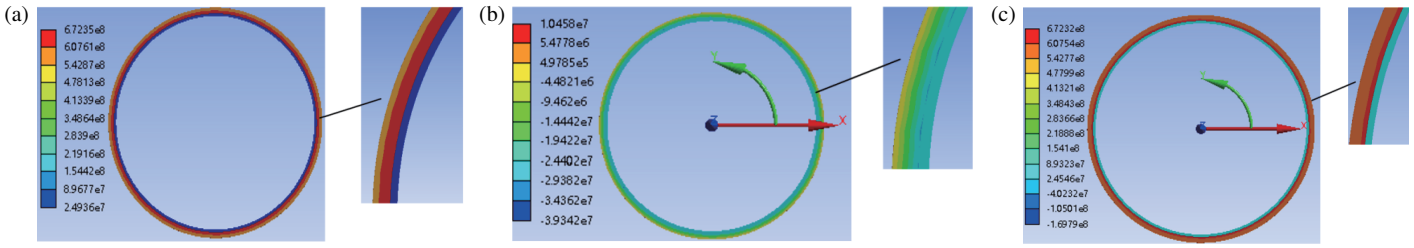


**FIGURE 14**. (a) Equivalent stresses (von Mises stresses) in the copper shield of the jacket strip. (b) Radial stresses in the copper shield of the jacket strip. (c) Tangential stresses in the copper shield of the jacket tape.

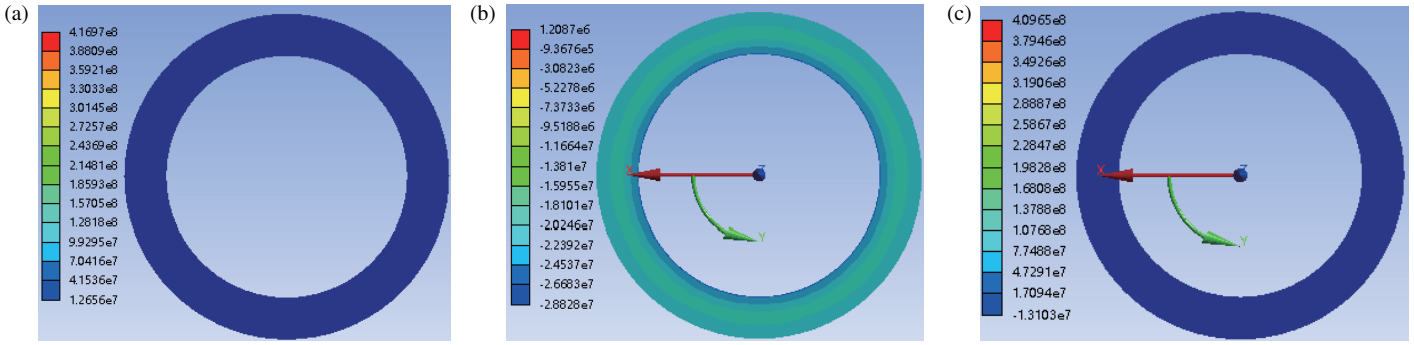


**FIGURE 15**. Stress distribution of permanent magnets. (a) Equivalent stresses in permanent magnets (von Mises stresses). (b) Radial stresses in permanent magnets. (c) Tangential stresses on permanent magnets.

The mechanical design constraints between the rotors are as follows:

(1) The maximum stress in the permanent magnet and the sheath does not exceed its allowable stress.

(2) The contact pressure between the permanent magnet and the sheath is large enough to transmit the electromagnetic torque. The rotor permanent magnet is subjected to contact pressure and centrifugal force, which is not considered in the design of this paper because the electromagnetic force is quite small compared to the mechanical loads of a high-speed machine. The maximum tensile stress of the permanent magnet is:

$$\sigma_{PM,\max} = \sigma_{PM,\omega} + \sigma_{PM,\rho}$$

where $\sigma_{PM,\max}$ is the maximum tensile stress in the permanent magnet $\sigma_{PM,\omega}$ from the centrifugal force and $\sigma_{PM,\rho}$ from the contact pressure between the permanent magnet and the sheath, both of which can be calculated.

The stress limit value of the permanent magnet is:

$$\sigma_{PM,\max} \leq [\sigma_{PM}]$$

where $\sigma_{PM}$ is the tensile allowable stress of the permanent magnet. The radial and tangential stresses of each rotor structure are obtained from Eq. (10), and the von Mises stress is obtained from Eq. (11).

The stresses on the sheath and copper shielding layer when the rotor is running at high speed, taking into account the temperature rise, are shown in Fig. 14. The equivalent stress of the sheath is $542.87 \sim 672.35$ Mpa; radial stress and tangential stress are $-29.38 \sim 5.48$ MPa and $542.77 \sim 672.32$ Mpa, respectively; the equivalent stress of the copper shield is $24.94 \sim 89.68$ Mpa; radial stress and tangential stress are $-39.34 \sim -24.40$ MPa and $24.55 \sim 89.32$ Mpa, respectively, all less than the maximum bearing capacity of each material, which are smaller than the maximum bearing force of each material. As can be seen from the figure, the size of the equivalent force on the sheath and copper shielding layer decreases gradually along the radius direction, with the maximum equivalent force on the inner surface of the sheath and the minimum equivalent force on the outer surface. Therefore, the multi-layer rotor structure with copper shielding layer can not only effectively reduce the eddy current loss, but also reduce the span of the stresses between the sheaths and improve the utilization of the sheaths to a certain extent.

Taking into account the temperature rise, when the rotor is running at high speed; the stress on the permanent magnet is shown in Fig. 15. The equivalent stress of the permanent magnet 12.66–41.54 MPa, radial stress $-18.10$–$26.68$ MPa, and tangential stress 17.09–13.10 Mpa, are less than 75 Mpa.

Figures 16–18 show the comparison between the results of analytical calculation of rotor stress and the results of finite element analysis. It can be seen from the figures that the radial stresses are continuously distributed on the boundary surface at each location. With the increase of the radius of the location of the stresses, the radial stresses start to decrease from the center of the rotor axis, then reach the minimum negative value of the maximum compressive pressure between the copper shielding layer and the protective sleeve, and finally increase to zero pressure on the outer surface of the protective sleeve. In contrast

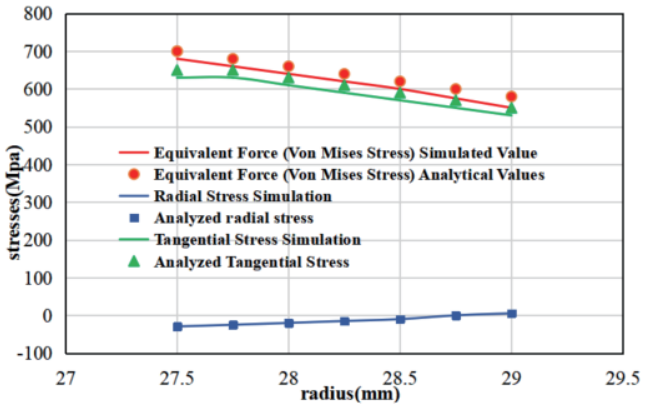


**FIGURE 16**. Comparison of stress distribution of sheath.

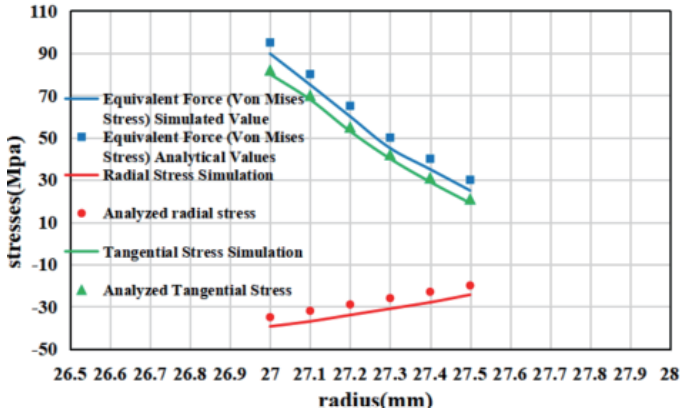


**FIGURE 17**. Comparison of stress distribution in copper shielding layer.

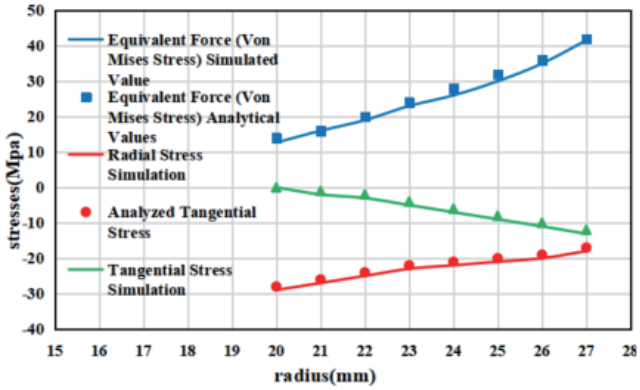


**FIGURE 18**. Comparison of stress distribution in permanent magnets.

to the radial stresses, the tangential stresses are not continuously distributed on the boundary surfaces, but they are continuously distributed in the radial direction inside each rotor part. In addition, the tangential stresses on the inside of the rotor part are greater than those on the outside, and the copper shield and jacket are subjected to tangential compressive stresses and the permanent magnet to tangential tensile stresses. The finite element simulation results for the permanent magnets show the same pattern as the analytical calculations, and the values are in general agreement with each other, with only a few errors. This is because the rotor is simplified to a two-dimensional ring when using analytical calculations, and the actual stresses at different locations in the axial direction are also somewhat different. The accuracy of the analytical calculation and finite element analysis is verified, which further proves the rationality of using copper shielding to suppress eddy current loss.

## 5. CONCLUSION

In this paper, a comprehensive research and analysis of high-speed motor rotor is carried out from multi-disciplinary electromagnetic characteristics, eddy current loss, and stress analysis to optimize the electromagnetic characteristics and eddy current loss while researching and analyzing the rotor strength.

(1) Three different rotor structures of high-speed permanent magnet synchronous motor models are constructed, and the simulation results of air gap magnetism, cogging torque, and output torque electromagnetic characteristics of the motor are compared by Maxwell finite element analysis, and the annular permanent magnet rotor structure is determined to be the optimal structure of high-speed frameless torque permanent magnet synchronous motor rotor.

(2) By comparing the rotor eddy current loss of carbon fiber sheath and alloy material sheath, the influence of material conductivity on the sheath and permanent magnet eddy current density is analyzed. To a certain extent, the larger the conductivity of the sheath is, the stronger the eddy current effect in the sheath is, the larger the eddy current loss is, and the stronger the inhibition effect on the eddy current loss of permanent magnet is, and the permanent magnet can be prevented from being demagnetized by too large an eddy current loss and too high a local temperature. By adding a copper shielding layer between the permanent magnet and the alloy sheath, the eddy current density of the permanent magnet is reduced from $2.26 \times 10^4$ A/m$^2$ to $1.91 \times 10^4$ A/m$^2$, further weakening the eddy current effect in the permanent magnet and reducing the eddy current loss in the permanent magnet.

(3) A two-dimensional model is constructed for analytical calculation of the loss-optimized rotor with copper shielding layer, and based on the theoretical model of thick-walled cylinder, the analytical formula for the stresses on the multilayer rotor structure is deduced. The three-dimensional structure of the rotor is also built for finite element analysis, and the results are compared with those of analytical calculation to verify the accuracy of analytical calculation and finite element analysis.

## ACKNOWLEDGEMENT

This work at Jiangxi University of science and technology was sponsored by the Jiangxi Provincial Key Discipline Technology and Technology Leader Training Program for Leading Talents Project under Grant Nos. 20213BCJ22019.

## REFERENCES

[1] Guo, K., Y. Guo, S. Fang, C. Li, and W. Xue, "Design and analysis of a permanent magnet frameless motor," *IEEE Journal of Emerging and Selected Topics in Power Electronics*, Vol. 12,

No. 3, 3124–3134, Jun. 2024.

[2] Zheng, J., Y. Guo, C. Xiao, X. Guo, and Y. Huang, "Research on frameless motor technology for joint module," in *IET Conference Proceedings*, Vol. 2020, No. 3, 819–824, 2020.

[3] Chen, Y., W. Hao, Y. Yang, L. Kang, and Q. Zhang, "Winding and electromagnetic analysis for 39-slot/12-pole frameless permanent magnet synchronous motor," in *2019 22nd International Conference on Electrical Machines and Systems (ICEMS)*, 1–6, Harbin, China, Dec. 2019.

[4] Zhang, Z., Z. Deng, Q. Sun, C. Peng, Y. Gu, and G. Pang, "Analytical modeling and experimental validation of rotor harmonic eddy-current loss in high-speed surface-mounted permanent magnet motors," *IEEE Transactions on Magnetics*, Vol. 55, No. 2, 1–11, Feb. 2019.

[5] Ou, J., Y. Liu, and M. Doppelbauer, "Comparison study of a surface-mounted PM rotor and an interior PM rotor made from amorphous metal of high-speed motors," *IEEE Transactions on Industrial Electronics*, Vol. 68, No. 10, 9148–9159, Oct. 2021.

[6] Woo, J.-H., T.-K. Bang, H.-K. Lee, K.-H. Kim, S.-H. Shin, and J.-Y. Choi, "Electromagnetic characteristic analysis of high-speed motors with rare-earth and ferrite permanent magnets considering current harmonics," *IEEE Transactions on Magnetics*, Vol. 57, No. 2, 1–5, 2020.

[7] He, T., Z. Q. Zhu, F. Xu, Y. Wang, H. Bin, and L. Gong, "Electromagnetic performance analysis of 6-slot/2-pole high-speed permanent magnet motors with coil-pitch of two slot-pitches," *IEEE Transactions on Energy Conversion*, Vol. 37, No. 2, 1335–1345, 2022.

[8] Xu, F., T. He, Z.-Q. Zhu, Y. Wang, S. Cai, H. Bin, D. Wu, L. Gong, and J. Chen, "Influence of slot number on electromagnetic performance of 2-pole high-speed permanent magnet motors with toroidal windings," *IEEE Transactions on Industry Applications*, Vol. 57, No. 6, 6023–6033, 2021.

[9] Yang, J. T., Z. Y. Wang, Y. J. Feng, and S. F. Huang, "Effect of rotor interference pattern on rotor stress in high-speed permanent magnet motors," *Journal of Electrotechnology*, Vol. 38, No. 16, 4263–4273, 2023.

[10] Shen, J. X., X. F. Qin, L. Yao, and Y. C. Wang, "Rotor strength analysis and sheath design for high-speed permanent magnet motors," *Chinese Journal of Electrical Engineering*, Vol. 42, No. 6, 2334–2345, Mar. 2022.

[11] Dong, C. Y., X. R. Li, Z. H. Yang, *et al.*, "Strength and dynamics of rotor of high-speed motor with segmented structure of permanent magnet and sheath," *Journal of Electrical Machines and Control*, Vol. 27, No. 3, 102–112, May 2023.

[12] Zhang, C., J. G. Zhu, and X. Y. Han, "Rotor strength analysis of high-speed surface-mounted permanent magnet motor," *Chinese Journal of Electrical Engineering Technology*, Vol. 38, No. 17, 4719–4727, 2016.

[13] Cheng, W. J., H. P. Geng, S. Feng, *et al.*, "Strength analysis of high-speed permanent magnet synchronous motor rotor," *Chinese Journal of Electrical Engineering*, Vol. 32, No. 27, 87–94, 2012.

[14] Gao, B. J., H. T. Liu, and L. K. Wang, "Analysis and calculation of three-dimensional electromagnetic field and eddy current loss of low-temperature and high-speed permanent magnet motor for LNG pump," *Chinese Journal of Electrical Engineering*, Vol. 40, No. 2, 634–644, 2020.

[15] Zhang, C., L. Chen, X. Wang, and R. Tang, "Loss calculation and thermal analysis for high-speed permanent magnet synchronous machines," *IEEE Access*, Vol. 8, 92 627–92 636, 2020.

[16] Tong, W. M., M. J. Hou, L. Sun, and S. J. Wu, "A method to analyze the rotor eddy current loss of high-speed permanent magnet motor with sheathed rotor based on an accurate subdomain model," *Journal of Electrotechnology*, Vol. 37, No. 16, 4047–4059, 2020.

[17] Zhuo, L., L. Sun, D. L. Shi, *et al.*, "Semi-analytical modeling and experimental validation of rotor eddy current loss in high-temperature, high-speed permanent magnet motors considering temperature variations," *Chinese Journal of Electrical Engineering*, Vol. 41, No. 24, 8305–8315, 2021.

[18] Zhang, Z., Z. Deng, Q. Sun, C. Peng, Y. Gu, and G. Pang, "Analytical modeling and experimental validation of rotor harmonic eddy-current loss in high-speed surface-mounted permanent magnet motors," *IEEE Transactions on Magnetics*, Vol. 55, No. 2, 1–11, 2019.

[19] Shen, J. X., T. Han, L. Yao, and Y. C. Wang, "Analysis of the effectiveness of increasing permanent magnet resistivity in reducing rotor eddy current losses in high-speed permanent magnet AC motors (in English)," *Journal of Electrotechnology*, Vol. 35, No. 9, 2074–2078, 2020.

[20] Chen, G. X., "Influencing factors of core and magnet losses in high-speed permanent magnet motors for air compressors," *Electrical Machines and Control Applications*, Vol. 47, No. 10, 61–67, 2020.